Chapter 2:

Enhancing Charge Transport Kinetics in Cobalt Molybdenum Oxide Nanorods via Iron-Doping for High-Performance Supercapacitors

Muhammad Arshad Kamran, Nimra Naeem, Suhaima

DOI: 10.21467/books.186.2
Additional information is available at the end of the chapter

The rapid advancements in the field of energy storage have rendered the supercapacitor as an integral element in moving towards sustainable energy systems. However, the commercial success of such energy storage systems is dependent on the production of electrode materials having both high conductivity and electrochemical stability. This chapter highlights the design and preparation of iron-doped cobalt molybdenum oxide ($CoMoO_4$) nanorods (NRs) as a potential solution for energy storage applications. The formation of NRs is carried out via a simple hydrothermal route, where the presence of iron (Fe) in the compound serves as a mediator in controlling the internal architecture for fast ion and electron transport. The NRs' crystallinity was verified using X-ray diffraction (XRD), while their characteristic vibrational modes were characterized through Raman spectroscopy. Scanning electron microscopy (SEM) was used to demonstrate the even dispersion of the iron in the $CoMoO_4$ NRs, while EDX was used to confirm that the different elements were uniformly distributed in the NRs. From all the materials tested, the 6% Fe-$CoMoO_4$ NRs had the most optimal electrochemical properties. Cyclic voltammetry performed at a 5 mVs^{-1} sweep rate produced a high specific capacitance of 2068 F g^{-1}, while the galvanostatic charge-discharge tests completed at a test current of 3 A g^{-1} also yielded a value of 2160 F g^{-1}. Using electrochemical impedance spectroscopy, a very low charge transfer resistance of 4.02 Ω was observed, which is significantly lower than that of the pure $CoMoO_4$ NRs, which had a charge transfer resistance of 9.72 Ω. The 6% Fe-$CoMoO_4$ NRs exhibited an energy density of 79.44 Wh kg^{-1} at 750 W kg^{-1} power and retained 87.13% capacitance over 3000 cycles. These results demonstrate that Fe-$CoMoO_4$ NRs are excellent candidates for integration into next-generation energy storage systems.

1. Introduction

In recent years, High-performance energy storage and conversion systems have been the subject of scientific research because fossil fuels are becoming less available and industries need more power [1-4]. Electrochemical devices like fuel cells, batteries, and supercapacitors are getting a lot of attention in both industries and academic research [5-10]. Supercapacitors (SC) are special because they combine the strengths of regular capacitors and batteries [11, 12]. They can be used in military equipment, pacemakers, and electric vehicles [13-15]. Their key advantages include longer cyclic stability, high power storage density, fast charge/discharge rates, and eco-friendliness [16-19]. Supercapacitors are divided into two types based on how they store charge: electric double-layer capacitors (EDLCs) and pseudocapacitors (PCs) [20-22]. PCs are especially promising because they have good electrochemical performance, long life, and high

ISBN: 978-81-998984-9-3

power and energy storage [23]. The performance of supercapacitors depends a lot on the materials used in the electrodes. So, it is essential to develop electrode materials with better shapes and structures. Transition metal oxides (TMOs) and polymers work well as electrode materials for PCs because they can change their oxidation states, have high capacitance, and low resistance [23, 24].

TMOs like cobalt oxide, molybdenum oxide, and zinc oxide are good for storing energy in supercapacitors [25, 26], Binary TMOs such as $ZnCo_2O_4$, $NiMoO_4$, and $CoMoO_4$ have drawn interest from numerous investigations because of their potent redox reactions and high electrical conductivity [27-29]. Among them, $CoMoO_4$ is promising because it is affordable, has good cycling stability, and strong redox activity [30-32]. Many studies have used $CoMoO_4$-based electrodes in supercapacitors. Xia et al. (2013) revealed a specific capacitance of about 394.5 F/g with an energy density of 54.8 Wh/kg for a composite of $CoMoO_4$ and graphene [33]. Nti et al. (2018) made a composite of $NiMoO_4$@$CoMoO_4$ nanorods with a high specific capacitance of about 1445 F/g [34]. Wang et al. (2016) found that a Co3O4@CoMoO4 core-shell electrode had a specific capacitance of almost 1902 F/g [35]. The majority of studies have concentrated on using CoMoO4-based materials to improve the specific capacitance. However, there hasn't been much work on using metal-doped CoMoO4 for supercapacitors. Doping, or adding other elements, is a useful method for enhancing the electrochemical properties of materials. Adding elements like alkali, transition, lanthanide, and post-transition metals can change properties like electrical conductivity, oxygen vacancies, and refractive index [36]. Transition-metal-doped CoMoO4 nanostructures can be used in different areas like sensing, lithium-ion battery anodes, supercapacitors, and breaking down ionic dyes [37-39]. Nanostructures such as rods, tubes, fibers, and wires are better than bulk materials because they have a larger surface area and more access to active sites, which reduces the distance charge carriers have to travel and improves redox capacity [23]. Among different ways to make these materials, the hydrothermal method is popular because it's easy, uses low temperatures, is safe, and can control the shape of the final product [40]. Notably, there is currently a lack of research specifically addressing the fabrication of iron-doped cobalt molybdenum oxide nanostructures for application as supercapacitor electrodes.

In this chapter, the hydrothermal method was used to synthesize undoped $CoMoO_4$ nanorods and Fe-doped $CoMoO_4$ nanorods for supercapacitor applications. The incorporation of iron (Fe) into $CoMoO_4$ modifies the surface morphology and enhances the electrochemical performance. Cyclic voltammetry (CV), galvanostatic charge-discharge (GCD) and electrochemical impedance spectroscopy (EIS) were used to test the electrochemical performance. The investigations were conducted using a three-electrode system in the presence of a 2M KOH solution as the electrolyte. The GCD outcomes revealed that the electrode fabricated from 6% Fe-$CoMoO_4$ nanorods possessed a specific capacitance of 2160 F/g, at the current density of 3 A/g, with an impressive energy and power density respectively, of 79.44 Wh/kg and 750 W/kg. This sample kept 87.13% of its initial capacitance after 3000 cycles. The present study provides a viable pathway for the application of Fe-doped $CoMoO_4$ NRs as a novel functional material in energy storage devices, particularly within the realm of high-performance supercapacitors.

ISBN: 978-81-998984-9-3

Book DOI: 10.21467/books.186

2. Experimentation

2.1. Synthesis Approach

Ammonium heptamolybdate ($(NH_4)_6Mo_7O_{24}$), Iron nitrate ($Fe(NO_3)_2$), Cobalt nitrate hexahydrate ($Co(NO_3)_2.6H_2O$), Ammonium fluoride (NH_4F), Urea ($Co(NH_2)_2$), activated carbon and nafion were brought from sigma Aldrich. Deionized water (D.I.) and ethanol were acquired from a scientific store. The hydrothermal approach was used to synthesize $CoMoO_4$ NRs and Fe-doped $CoMoO_4$ NRs. Typically (2, 4, and 6 mol % of cobalt nitrate hexahydrate) $Fe(NO_3)_2$, 0.267 g $(NH_4)_6Mo_7O_{24}$, 0.441 g $Co(NO_3)_2{\cdot}6H_2O$, and an appropriate amount of NH_4F were mixed into 30 ml deionized water on the magnetic stirrer for 10 minutes at room temperature. On the other side, 0.3621 g $Co(NH_2)_2$ was mixed into 10 ml deionized water on a magnetic stirrer transferred into a burette and added slowly into the mixture of ammonium molybdate and cobalt nitrate. The prepared mixture was further stirred for an hour to make a pink homogenous mixture. After that, the pink homogenous solution was put into a 50 mL stainless-steel autoclave lined with Teflon, and it was kept at 180 °C for 12 hours in a temperature-controlled oven. After hydrothermal treatment, the obtained solution was filtered and washed with deionized water and ethanol for the removal of residues. The obtained precipitates were dried at 60 ℃ for 10 hours and primeval $CoMoO_4$ NRs were obtained. Then these precipitates were calcinated at 500 ℃ for 2 hours.

2.2. Diagnostic Technique

A variety of the techniques were used to study the properties of electrode material as-synthesized. The structural morphology was examined using X-ray diffractometer (Model: Tongda TD-3700) with the 2θ range of 20° to 60° and the radiations were the Cu-k a-radiation (1.5406 Å). Doping of the material was verified with the help of GMD PROTRUSTECH Raman spectrometer. Scanning electron microscope (SEM) (Model: MAIA3 TESCAN) was used to analyze the surface morphology of the synthesized electrode material. The absorption spectra were studied with a UV-visible spectrophotometer (Model C7200) in the 350-900 nm range. GAMRY Potentiostat Interface 5000 (Model: 14543) was used to observe the electrochemical performance of synthesized electrode material.

2.3. Electrode Preparation

The working electrodes were prepared with a weight of 85% of the active mass ($CoMoO_4$ NRs and Fe-doped $CoMoO_4$ NRs), 10% activated carbon, and 5% Nafion. First, the slurry of active material and activated carbon was made and then it was compressed on nickel foam ($1x1cm^2$). Then this nickel foam was dried at 60℃ for 3 hours. Around 2 mg of the active material was loaded on each electrode. The platinum and Ag/AgCl electrodes were considered the counter electrode (CE) and the reference electrode (RE) respectively in the three-electrode set up. All electrochemical measurements were done using a 2 M KOH alkaline solution as the electrolyte. CV, constant-current GCD, and electrochemical impedance spectroscopy (EIS) were used to examine the electrochemical performance of the fabricated electrode.

3. Results and Discussion

3.1. Structural Analysis

3.1.1. X-ray Diffraction

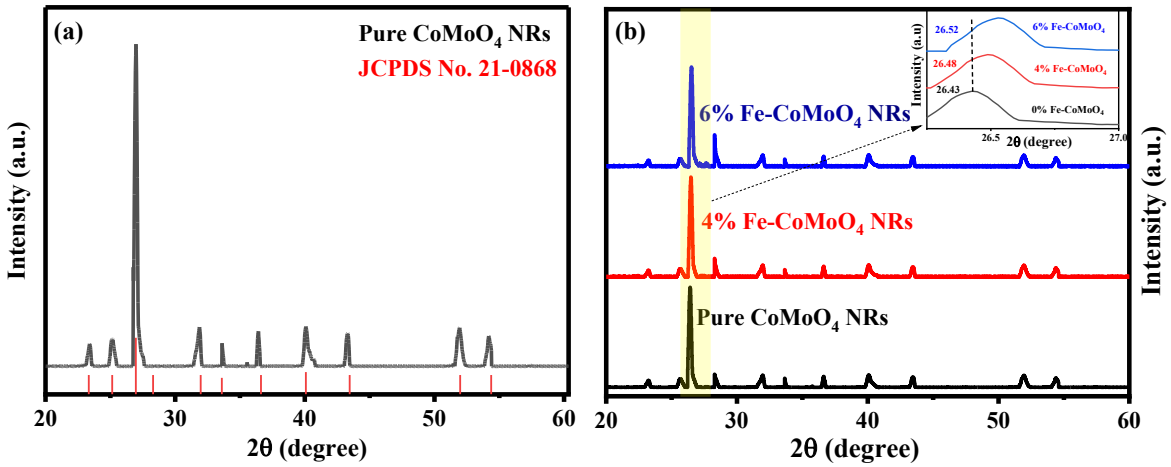

Figure 2.1. The XRD pattern of; (a) $CoMoO_4$ NRs is well indexed with JCPDS No. 21-0868; (b) comparison of XRD pattern of $CoMoO_4$ NRs, 4% Fe-$CoMoO_4$ NRs, and 6% Fe-$CoMoO_4$ NRs.

X-ray diffraction (XRD) served to characterize the phase and crystalline structure of the prepared electrode materials. The XRD pattern of $CoMoO_4$ NRs, 4% Fe-$CoMoO_4$ NRs, and 6% Fe-$CoMoO_4$ NRs are depicted in **Figure 2.1** (a, b). All of the defined peaks belong to planes (021), (201), (002), (301), (022), (222), (400), (003), (113), (204), and (440) corresponding to $2\theta_{23.24}$, $2\theta_{25.69}$, $2\theta_{26.43}$, $2\theta_{28.30}$, $2\theta_{31.97}$, $2\theta_{33.65}$, $2\theta_{36.64}$, $2\theta_{40.08}$, $2\theta_{43.46}$, $2\theta_{51.98}$, and $2\theta_{54.38}$, respectively. Every peak that was seen aligned with JCPDS card No. 21-0868 and confirmed the monoclinic phase of the synthesized material [41-43]. In addition to this, no other peaks were detected which confirms the high purity of $CoMoO_4$ NRs. The characteristic peak at $2\theta_{26.43}$ slightly shifted towards a higher angle from 26.43^0 to 26.52^0, which is shown in the inset graph of **Figure 2.1**. The red shift in the characteristic peak confirms the successful doping in $CoMoO_4$ NRs. This shift is due to the greater ionic radius of dopant material that expands the unit cell volume and produces a redshift [44]. The sharpness of the observed peak of synthesized electrode material represents its crystalline nature. The Debye-Scherrer formula provided the average crystallite size (D) of the resulting electrode samples, as shown in **Equation 2.1** [45-47].

$$D = \frac{K\lambda}{\beta \cos\theta} \qquad (2.1)$$

Where the value of k depends on the crystal structure (monoclinic = 0.89), λ represents the X-ray wavelength of Cu Kα radiation (λ = 1.5406 Å), and θ is the diffraction angle. The average crystallite size of the $CoMoO_4$ NRs was observed to be reduced by increasing the concentration of Fe. The computed

crystallite sizes are 35.54, 35.31, and 35.25 nm for undoped $CoMoO_4$ NRs, 4% Fe-$CoMoO_4$ NRs, and 6% Fe-$CoMoO_4$ NRs, respectively.

3.1.2. Raman Analysis

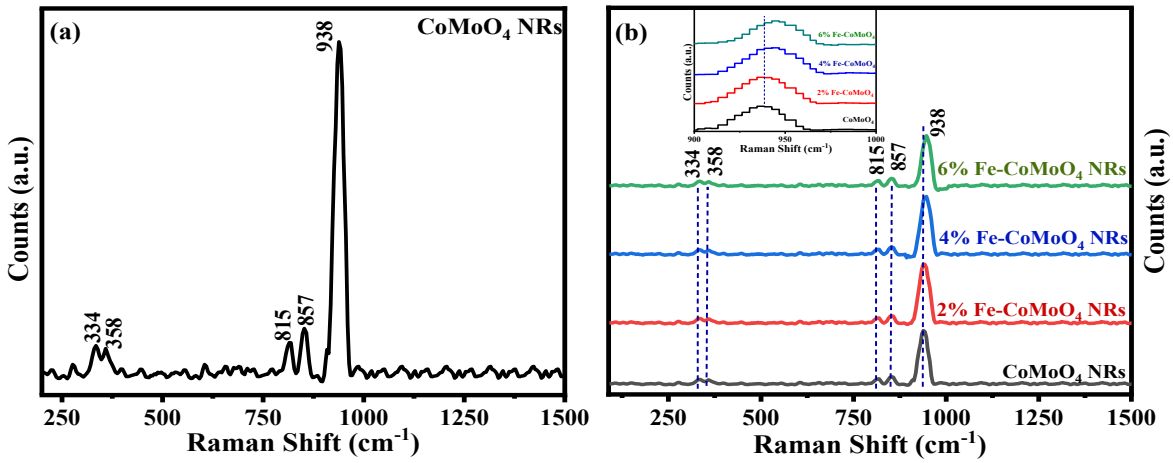

Figure 2.2. The Raman Spectrum of; (a) $CoMoO_4$ NRs; (b) The comparison Raman spectrum of $CoMoO_4$ NRs, 4% Fe-$CoMoO_4$ NRs, and 6% Fe-$CoMoO_4$ NRs.

The Raman analysis was used for the confirmation of the Fe-doping in $CoMoO_4$ NRs, and the observed spectra of $CoMoO_4$ NRs, 2%, 4%, and 6% Fe-doped $CoMoO_4$ NRs are shown in **Figure 2.2** (a, b). The sharpness of the peaks in the Raman spectrum revealed that the nanorods were dispersed randomly. At room temperature, Raman spectra of pure $CoMoO_4$ NRs and Fe-doped $CoMoO_4$ NRs were performed within the range of 109-1500 cm^{-1}. There are five Raman bands 815, 857, 938, 334, and 358 cm^{-1} were observed in the Raman spectrum of pure and Fe-doped $CoMoO_4$ NRs. The bands at 815 cm^{-1} and 857 cm^{-1} were associated with the O-Mo-O bond, and the strong double at 938 cm^{-1} might be attributed to Mo=O. Furthermore, the Co-O-Mo bond may be assimilated to the peaks at 334 cm^{-1} and 358 cm^{-1} [48-50]. The sharp peak at 938 cm^{-1} was found to shift towards a higher wavenumber that confirms the Fe-doping into $CoMoO_4$ NRs which is presented in the inset graph of **Figure 2.2** (b).

3.2. Morphology and Elemental Composition.

3.2.1. Scanning Electron Microscopy (SEM)

SEM was used to examine the surface morphology of synthesized $CoMoO_4$ and Fe-doped $CoMoO_4$ electrode materials. SEM micrographs revealed that $CoMoO_4$, 4% Fe-CoMoO4, and 6% Fe-$CoMoO_4$ exhibit rod-like morphology as shown in **Figure 2.3** (a_1-c_1) [51]. These rods are within the nanoscale range, as depicted in the histogram presented in **Figure 2.3** (a_2-c_2). Notably, the surface of the $CoMoO_4$ NRs appears rough, while the addition of Fe transforms it into a smoother and finer surface, accompanied by a decrease in diameter that enhances the surface-to-volume ratio. This observed morphology of Fe-doped $CoMoO_4$ NRs is considered advantageous, as it provides more area for redox reactions in energy storage applications, particularly supercapacitors.

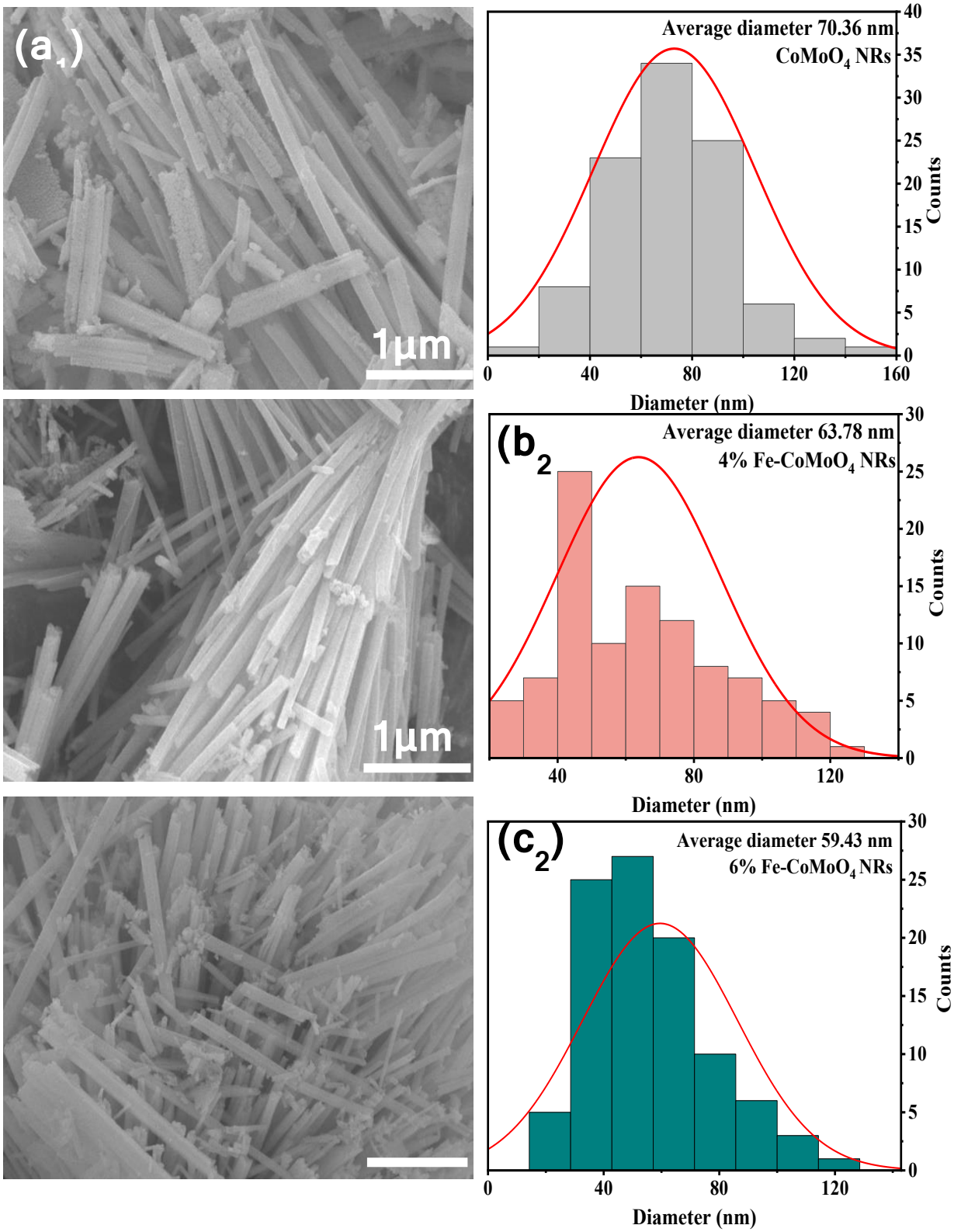

Figure 2.3. The SEM micrograph of; (a_1) $CoMoO_4$ NRs, (b_1) 4% Fe-$CoMoO_4$ NRs, and (c_1) 6% Fe-$CoMoO_4$ NRs, (a_2, c_2) Histogram to show the diameter of NRs

3.2.2. Elemental Composition Analysis

The energy dispersive X-ray (EDX) spectroscopy was conducted to examine the elemental composition of the prepared electrode materials. The EDX spectrum of $CoMoO_4$ NRs contained characteristic peaks corresponding to Co, Mo, and O, Validating the synthesis of $CoMoO_4$ NRs, as shown in **Figure 2.4** (a)**.** It is also observed that no other elements were found in the sample because no extra peaks were detected, confirming the high purity of the synthesized material. The EDX spectrum of 4% Fe-doped $CoMoO_4$ NRs and 6% Fe-doped $CoMoO_4$ NRs exhibited characteristic peaks associated with Co, Mo, Fe, and O elements. Only one additional peak, associated with the dopant material (Fe), was observed, as shown in **Figure 2.4** (b-c)**.** The weight percentages of each element present in $CoMoO_4$ NRs, 4% and 6% Fe-doped $CoMoO_4$ NRs, are listed in **Table 2.1.**

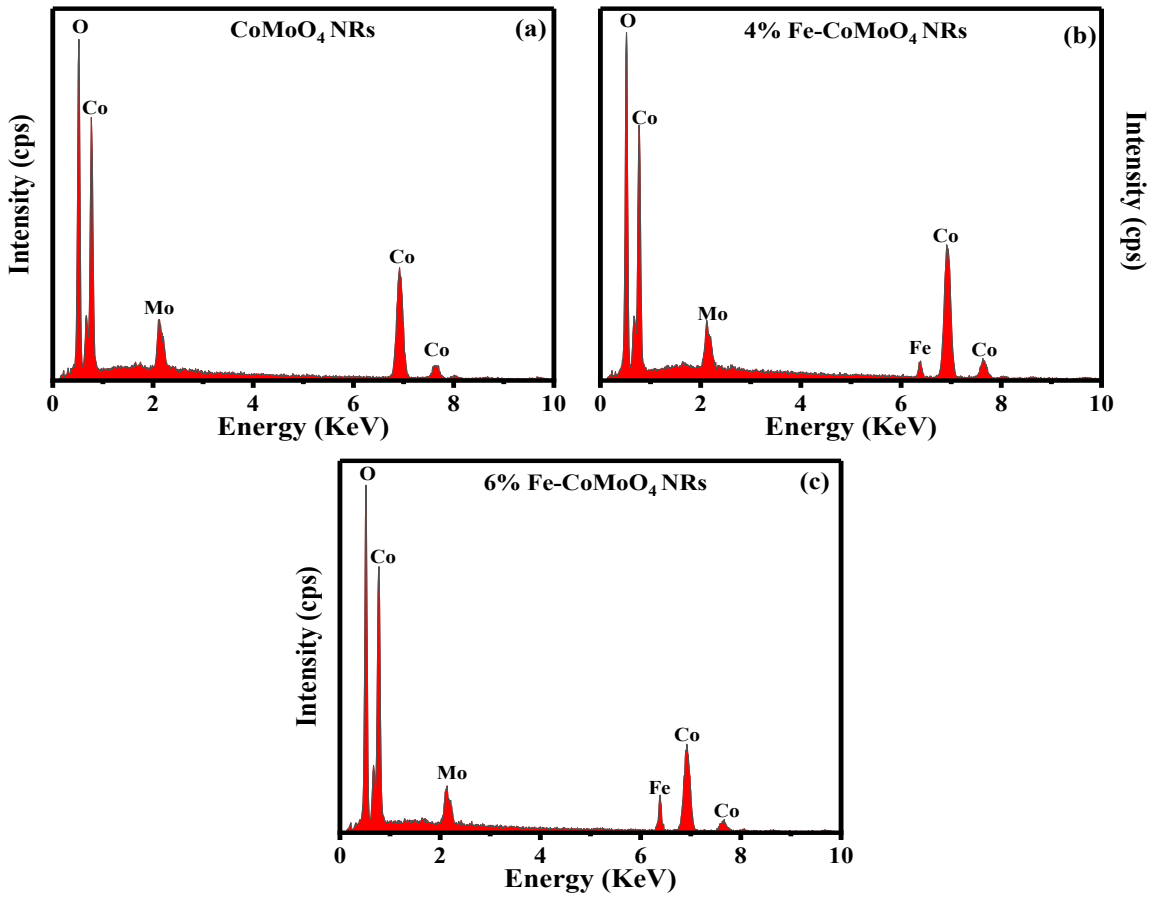

Figure 2.4: Energy dispersive X-ray spectrum of; (a) $CoMoO_4$ NRs, (b) 4% Fe-$CoMoO_4$ NRs, and (c) 6% Fe-$CoMoO_4$ NRs.

Table 2.1. The weight % of each element present in the synthesized electrode materials.

Electrode Material	Fe (Wt %)	Co (Wt %)	Mo (Wt %)	O (Wt %)
$CoMoO_4$ NRs	0	50.71	9.58	39.71
4% Fe-$CoMoO_4$ NRs	2.55	48.23	10.56	38.66
6% Fe-$CoMoO_4$ NRs	4.89	47.13	10.12	37.96

3.3. Optical Analysis

Adsorption, the process of promoting the electrons of the prepared specimen to a higher energy level, requires a specific amount of light energy (measured in nm). When monochromatic light strikes the synthetic material, atomic electrons absorb it and continue to do so until they enter their excited states, which results in an adsorption peak. The UV-Vis spectrometer (MODEL: C7200) was used to examine the optical behavior of the synthesized $CoMoO_4$ NRs and Fe-doped $CoMoO_4$ NRs. The synthesized samples were scanned at the speed of 480 nm/min and within the range of 350-900 nm.

Four samples, including undoped $CoMoO_4$ NRs and Fe-doped $CoMoO_4$ NRs with different Fe concentrations (2%, 4%, and 6%), were analyzed. The solutions of undoped $CoMoO_4$ NRs, 2% Fe-doped $CoMoO_4$ NRs, 4% Fe-doped $CoMoO_4$ NRs, and 6% Fe-$CoMoO_4$ NRs were prepared in acetone as a solvent at ambient temperature. In the absorption spectra of $CoMoO_4$ NRs, two noticeable broad absorption bands were observed which are shown in **Figure 2.5** (a). No other peaks were observed except for these two broad bands, confirming that $CoMoO_4$ NRs exhibit good optical properties. The observed peaks shift towards higher wavelengths due to the doping effect of Fe in $CoMoO_4$ NRs, as shown in **Figure 2.5** (b). Tauc equation is used to calculate the energy bandgap of the fabricated materials shown in **Equation 2.2** [52].

$$(\alpha h\upsilon)^n = C\ (h\upsilon - E_g) \qquad (2.2)$$

Where **C** represents constant, **υ** associated with photon energy, **α** is the molar extinction coefficient, and **n** may be 1/2, or 2 for indirect, or direct transitions, respectively, depending on the type of transition [53]. The direct bandgap of $CoMoO_4$ NRs, 2% Fe-$CoMoO_4$ NRs, 4% Fe-$CoMoO_4$ NRs, and 6% Fe-$CoMoO_4$ NRs is 3.34, 3.21, 3.15, and 2.98 eV, respectively and the relation of band gap with doping concentration is shown in **Figure 2.5** (d). When the concentration of Fe rises, the optical energy band gap shrinks. Tauc's plot of $CoMoO_4$ NRs and Fe-doped $CoMoO_4$ NRs is shown in **Figure 2.5** (c). The UV-Vis absorption spectra of the doped sample showed higher light absorption and a pronounced red shift when compared to the virgin material, showing that the dopant was successfully incorporated. The smaller optical band gap

allows for better charge carrier excitation and transfer. These properties facilitate quicker electron transport and inhibit charge recombination, improving the electrode's electrochemical performance.

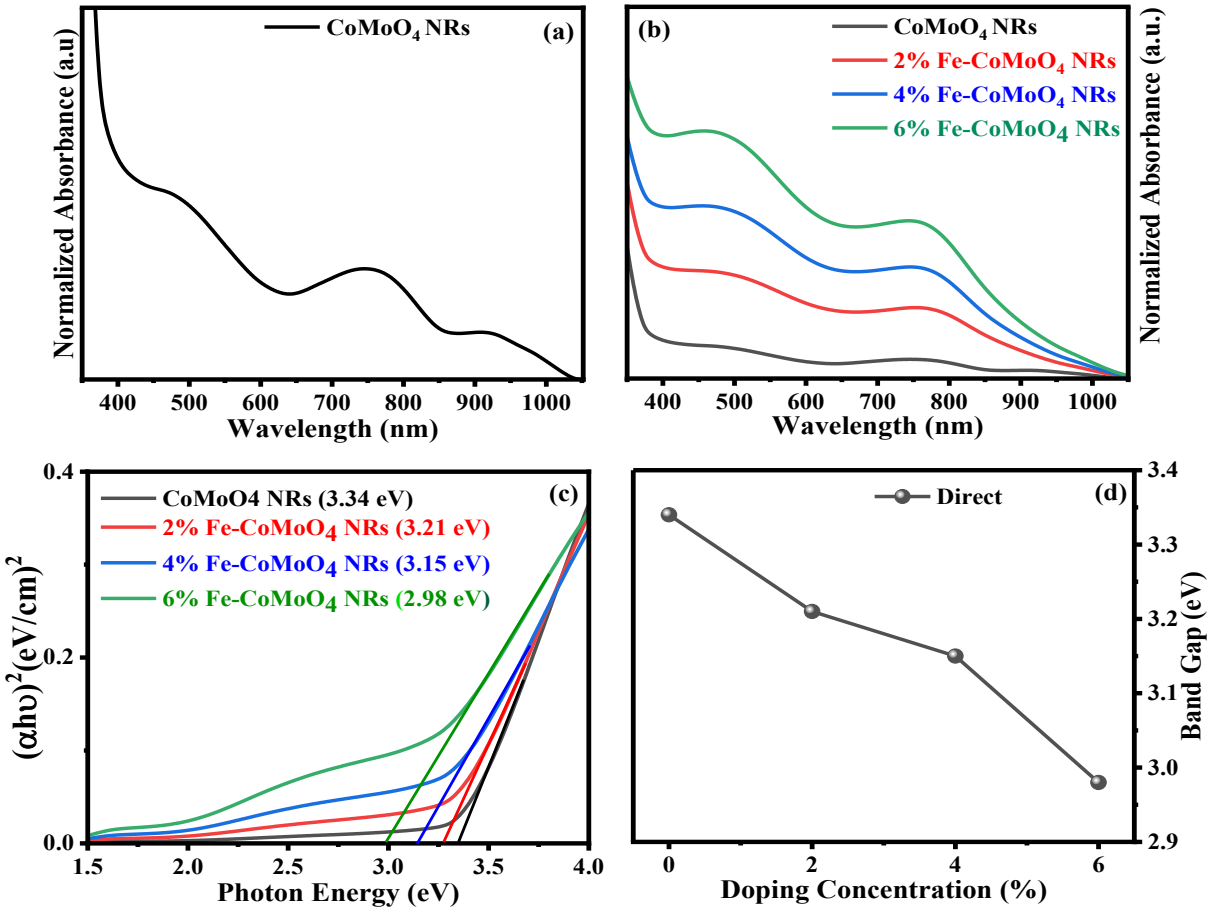

Figure 2.5. The normalized absorbance spectrum of; (a) $CoMoO_4$ NRs; (b) The comparison of the normalized absorbance spectrum of $CoMoO_4$ NRs, 2% Fe-$CoMoO_4$ NRs, 4% Fe-$CoMoO_4$ NRs, and 6% Fe-$CoMoO_4$ NRs; (c) The Tauc plot of $CoMoO_4$ NRs, 2% Fe-$CoMoO_4$ NRs, 4% Fe-$CoMoO_4$ NRs, and 6% Fe-$CoMoO_4$ NRs; (d) The comparison of direct band gap and doping concentration of Fe in $CoMoO_4$ NRs.

3.4. Electrochemical Investigation

3.4.1. Cyclic Voltammetry

In the three-electrode configuration, cyclic voltammetry was used to check out the nature of the materials and to calculate the value of specific capacitance exhibited by the materials. The CV measurements of undoped $CoMoO_4$ NRs, 4% Fe- $CoMoO_4$ NRs, and 6 % Fe- $CoMoO_4$ NRs were carried out at different scan speeds of 5mV s^{-1}, 10 mV s^{-1}, 15 mV s^{-1}, 25mV s^{-1}, 50mV s^{-1} and 100 mV s^{-1} with an operating potential window (PW) -0.2 to 0.6 eV are shown in **Figure 2.6** (a-c). The cyclic voltammograms of each sample express the noticeable redox peak at the potential that indicates the pseudocapacitive nature of the prepared

materials. The volumetric current increased as the scan rates increased. This suggested that the kinetics of the interfacial redox processes, as well as the rates of ionic and electronic transport, were sufficient [54]. The area enclosed by the cyclic voltammogram of 6 % Fe-doped $CoMoO_4$ NRs is greater than the 4 % Fe-$CoMoO_4$ NRs and undoped $CoMoO_4$ NRs which demonstrated that it has greater specific capacitance. The electrode has strong reversibility and charge storage capacity since the area of the CV curves rose as the scan speed increased. **Equation 2.3** is used to determine the specific capacitance (Cs) of synthetic electrode materials.

$$C_s = \frac{A}{2KmΔV} \qquad (2.3)$$

Where **A** is the absolute area under the voltammogram, **ΔV (V_2-V_1)** is the potential window of the voltammogram, m is the mass of active electrode material and **K** is the scan rate of CV curves. **Figure 2.6 (d)** demonstrates the value of scan rate of specific capacitance of each electrode material. The C_s value of 2068 F g^{-1} at a scan rate of 5 mV s^{-1} is the largest on the electrode made with 6 % Fe-doped CoMoO4 NRs. The C_s value of each sample at different scan rates is listed in Table 2.2.

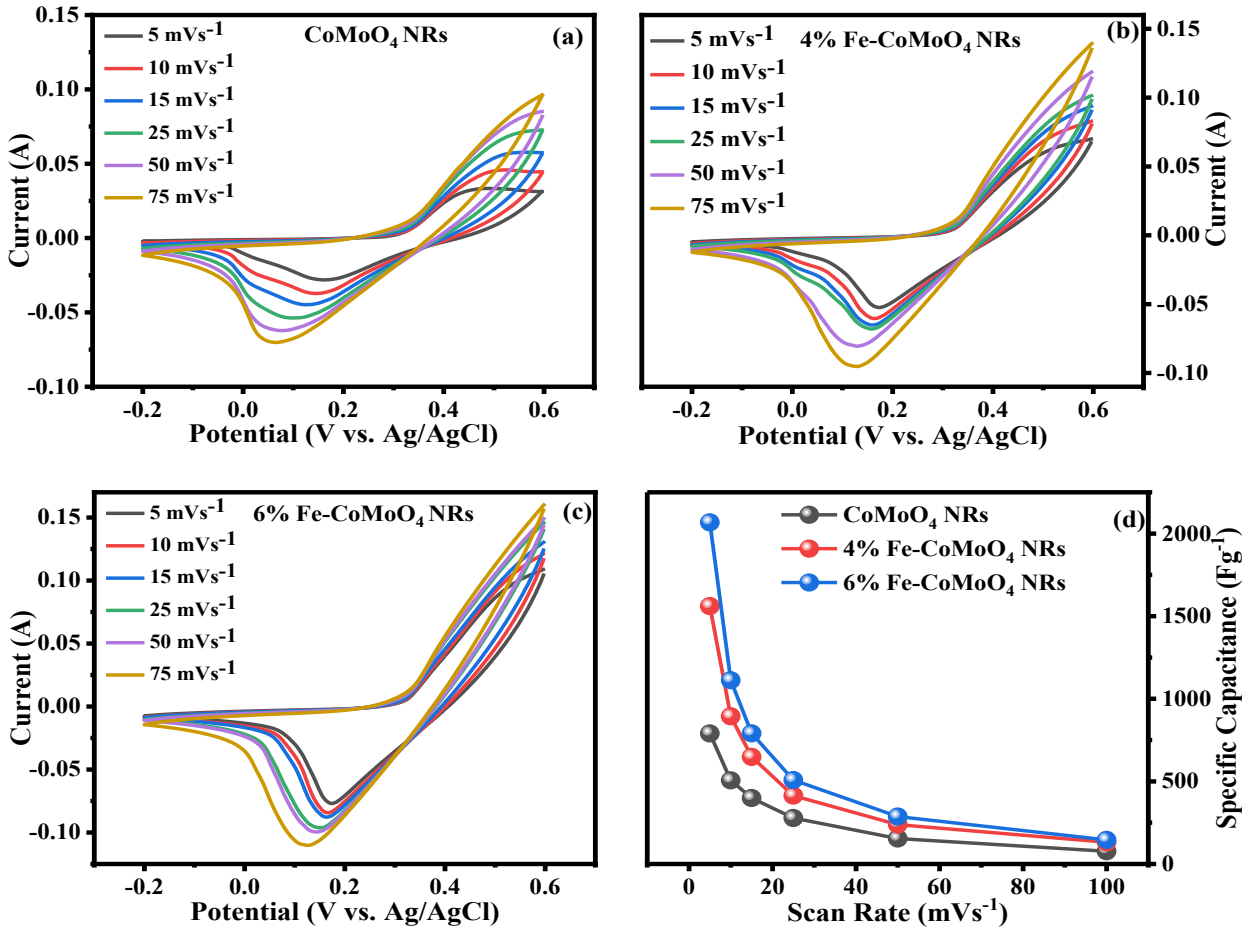

Figure 2.6. The Cyclic Voltammogram (CV) of; (a) $CoMoO_4$ NRs, (b) 4% Fe-$CoMoO_4$ NRs, and (c) 6% Fe-$CoMoO_4$ NRs at different scan rates; (d) The comparison of specific capacitance of each electrode at different scan rates.

ISBN: 978-81-998984-9-3

Book DOI: 10.21467/books.186

Table 2.2. Specific capacitance value calculated from CV curves of the synthesized electrode materials at different scan rates.

Electrode Material	5 mVs^{-1}	10 mVs^{-1}	15 mVs^{-1}	25 mVs^{-1}	50mVs^{-1}	100 mVs^{-1}
$CoMoO_4$ NRs	790	506	399	278	154	77
4% Fe-$CoMoO_4$ NRs	1561	894	648	414	238	132
6% Fe-$CoMoO_4$ NRs	2068	1112	791	508	287	146

3.4.2. Galvanostatic Charge Discharge (GCD) Curves

The GCD curves were used to explore the further electrochemical properties of synthesized electrode material. It was confirmed that the shapes of all the GCD curves at varying current densities of 3 A^{-1}, 4 A g^{-1}, 5 A g^{-1} and 6 A g^{-1} were non-linear confirming that the synthesized materials were pseudocapacitive [54]. **Figure 2.7 (a-c)** illustrates all the GCD curves obtained. **Equation (2.4-2.6)** was used to calculate the values of specific capacitance (C_s), power density (P_d) and energy density (E_d).

$$C_s = \frac{I \times \Delta t}{\Delta V \times m} \quad (2.4)$$

$$E_d = \frac{C_p \times (\Delta v)^2}{2 \times 3.6} \quad (2.5)$$

$$P_d = \frac{E_d \times 3600}{\Delta t} \quad (2.6)$$

Where *I* is the discharging current (A), **Δt** is the discharge time (s), m is the active mass (g), and **ΔV** is the discharge potential window [55]. Among all samples, GCD curves for 6% Fe-$CoMoO_4$ NRs exhibited more discharging time in comparison with pure $CoMoO_4$ NRs and 4% Fe-$CoMoO_4$ NRs. The optimized electrode material (6% Fe-$CoMoO_4$) exhibited the C_s value of about 1200, 1800, 2000, and 2160 F g^{-1} at current densities 3, 4, 5, and 6 A g^{-1}, respectively.

Figure 2.7 (d-e) depicts the relationship between C_s and discharge time, as well as current density. It is observed that the C_s value of each electrode increases as the current density decreases. The energy dissipation time increases which provides a large surface area for OH– ions for Faradaic reactions to take place [21]. The highest value of the C_p attained from GCD plateau at 3 A g^{-1} was 2160 F g^{-1} which corresponds to the specific capacitance (2068 F g^{-1}) value attained from the CV graph. In addition, the power density and energy density of the same were 750 W kg^{-1} and 79.44 Wh kg^{-1} respectively. The optimized electrode 6% Fe-$CoMoO_4$ NRs, exhibits remarkable cycle stability even at a current density of 3

A g^{-1}, retaining 87.13 % of its initial specific capacitance after 3000 cycles, as depicted in **Figure 2.7** (f). The computed values from the GCD curves of C_s, E_d, and P_d are displayed in **Table 2.3**.

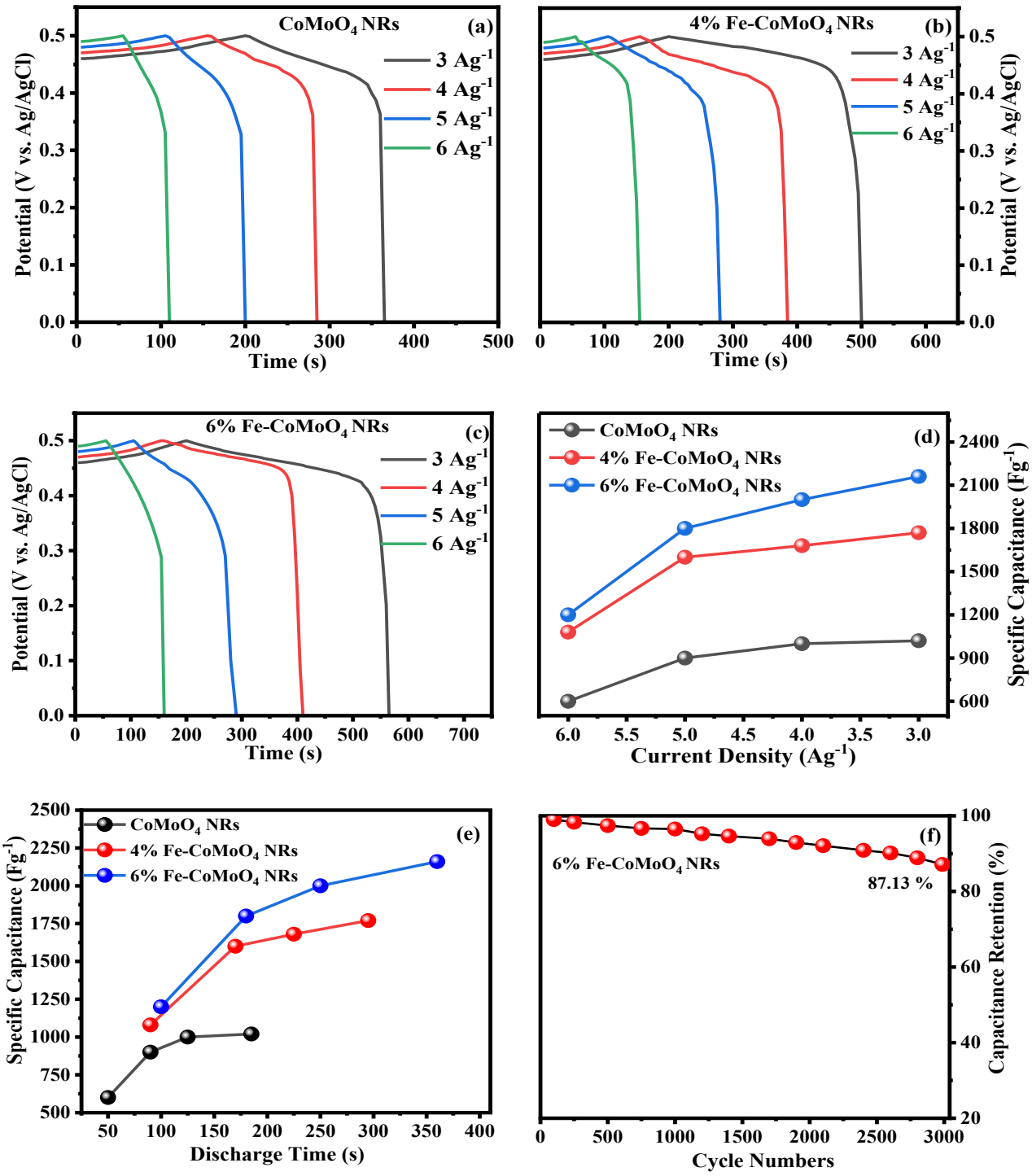

Figure 2.7. The Galvano static charge-discharge (GCD) curves of; (a) $CoMoO_4$ NRs, (b) 4% Fe-$CoMoO_4$ NRs, and (c) 6% Fe-$CoMoO_4$ NRs at different current densities; (d-e) The comparison of specific capacitance of each electrode at different current densities and discharge time; (f) The cyclic performance of 6% Fe-$CoMoO_4$ NRs.

Table 2.3. The values of specific capacitance, energy density, and power density of the synthesized electrode material at different current densities.

Electrode Material	Discharge Time (s)	Current Density (A g^{-1})	Specific Capacitance (F g^{-1})	Energy Density (Wh kg^{-1})	Power Density (W kg^{-1})
$CoMoO_4$ NRs	185	3	1020	35.41	750
	125	4	1000	34.72	1000
	90	5	900	31.25	1250
	50	6	600	20.83	1500
4% Fe-$CoMoO_4$ NRs	295	3	1770	61.45	750
	225	4	1680	58.33	1000
	170	5	1600	55.55	1250
	90	6	1080	37.5	1500
6 % Fe-$CoMoO_4$ NRs	360	3	2160	79.44	750
	250	4	2000	75	1000
	180	5	1800	62.5	1250
	100	6	1200	41.66	1500

3.4.3. Electrochemical Impedance Spectroscopy (EIS)

In this study, EIS was used to examine the electrical conductivity characteristics of electrode materials intended for supercapacitors. The frequency spectrum of the impedance behavior of $CoMoO_4$ NRs, 4% Fe-$CoMoO_4$ NRs and 6% Fe-$CoMoO_4$ NRs electrodes was observed with Nyquist plots with equivalent circuit fitting diagrams between 0.1 Hz and 100 kHz as shown in **Figure 2.8** (a-c). The segment of the plot at which the high-frequency component intersects the real axis represents the internal resistance of the electrodes [56]. The charge-discharge resistance (R_{ct}) is the high-frequency component of the impedance that is due to the Faraday reaction and the double-layer capacitance (C_{dl}) of the surface. This indicates the resistance to diffusion of ions at the electrode-electrolyte interface. The linearly low-frequency part can be attributed to the Warburg impedance (Z), which is the resistance to diffusion of the electrolyte [57, 58]. It is observed from **Table 2.4** that the 6% Fe-$CoMoO_4$ electrode material demonstrates reduced internal resistance, implying high electrolyte conductivity. The linear portion of the Nyquist plot indicates ion diffusion resistance between the electrolyte and electrode surface, with 6% Fe-$CoMoO_4$ NRs showing

minimal diffusion resistance, helping to speed up diffusion rates. The smooth and fine surface of 6% Fe-$CoMoO_4$ NRs enhances electrode cycling stability and promotes redox reactions.

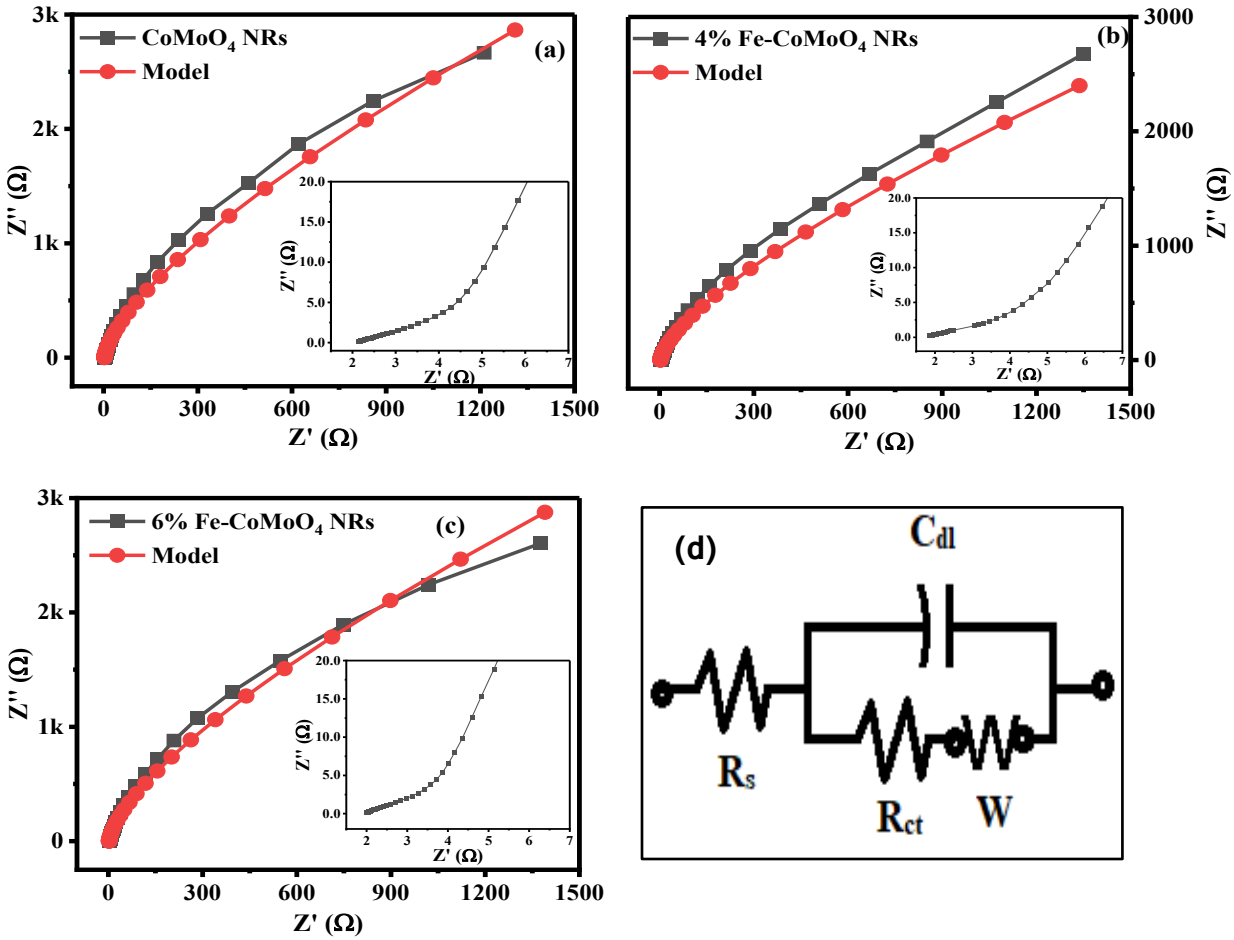

Figure 2.8. The Nyquist plot; (a) $CoMoO_4$ NRs, (b) 4% Fe-$CoMoO_4$ NRs, and (c) 6% Fe-$CoMoO_4$ NRs within the frequency range of 0.1-100 K Hz fitted with Warburg model. (d) The circuit diagram of the Warburg model.

ISBN: 978-81-998984-9-3

Book DOI: 10.21467/books.186

Table 2.4. The measurements for electrolyte resistance (R_s), double layer capacitance (C_{dl}), charge transfer resistance (R_{ct}), and Warburg impedance (Z) of 6% Fe-$CoMoO_4$ NRs.

Electrode Material	Electrolyte Resistance (Ω)	Double Layer Capacitance (μF)	Charge Transfer Resistance (Ω)	Warburg Impedance (Ω $s^{-1/2}$)
$CoMoO_4$ NRs	2.97	0.000314	9.72	0.000353
4% Fe-$CoMoO_4$ NRs	2.76	0.000292	7.97	0.000272
6% Fe-$CoMoO_4$ NRs	2.56	0.000282	4.02	0.000263

4. Conclusion

In summary, this study successfully demonstrates the first-ever fabrication of Fe-doped $CoMoO_4$ NRs via a facile hydrothermal approach. The integration of iron into the $CoMoO_4$ lattice proved to be a transformative strategy, yielding a unique one-dimensional architecture that significantly enhances charge transport kinetics. Electrochemical analysis indicated that the optimized electrode material (6% Fe-$CoMoO_4$ NRs) exhibited a remarkable specific capacitance of approximately 2068 F g^{-1} at 5 mV s^{-1}. The GCD curves of the optimized electrode material demonstrated a high specific capacitance of 2160 F g^{-1} at 3 A g^{-1}, coupled with a noticeable energy density of 79.44 Wh kg^{-1} and a high-power density of 750 W kg^{-1}. Moreover, the optimized electrode retained 87.13% of its initial capacitance after 3000 cycles. The remarkable electrochemical performance of 6% Fe-doped $CoMoO_4$ nanorods suggests that the synthesized electrode material serves as a novel candidate for supercapacitor applications. This research highlights the feasibility of transition metal doping as an effective strategy for the synthesis of efficient functional materials for the energy storage arena.

Publisher's Note

AIJR remains neutral with regard to jurisdictional claims in published maps and institutional affiliations.

Author's Detail

Muhammad Arshad Kamran*, Nimra Naeem, Suhaima
Department of Physics, University of Okara, Okara, Pakistan.

*Corresponding author

How to Cite this Chapter:

M. A. Kamran, N. Naeem, Suhaima, "Enhancing Charge Transport Kinetics in Cobalt Molybdenum Oxide Nanorods via Iron-Doping for High-Performance Supercapacitors," in *Emerging Functional Materials for a Sustainable Energy Future*, M. A. Kamran, Ed. India: AIJR Publisher, 2026, pp. 27-43. ISBN: 978-81-998984-9-3, doi: 10.21467/books.186.2

References

[1] W. A. Abbas *et al.*, "Recent advances in the use of TiO2 nanotube powder in biological, environmental, and energy applications," *Nanoscale Advances,* vol. 1, no. 8, pp. 2801-2816, 2019.

[2] B. Luo, D. Ye, L. Wang, "Recent Progress on Integrated Energy Conversion and Storage Systems" *Adv. Sci*. 2017, 4, 1700104. https://doi.org/10.1002/advs.201700104

[3] A. A. İnada, S. Arman, and B. Safaei, "A novel review on the efficiency of nanomaterials for solar energy storage systems," *Journal of Energy Storage,* vol. 55, p. 105661, 2022.

[4] M. Z. Iqbal, F. Alam, S. Alam, J. Khan, A. Ali, and M. Alzaid, "Synergetic electrochemical performance of strontium phosphate/polyaniline/graphene for high performance supercapattery devices," *Diamond and Related Materials,* vol. 124, p. 108918, 2022.

[5] C. A. Manrique-Escobar, M. Sparano, and M. Sorrentino, "Fuel cell plug-in hybrid electric vehicle thermal management strategy in parking time for low-temperature environments," *Journal of Energy Storage,* vol. 56, p. 106020, 2022.

[6] C. Ni *et al.*, "A B-site doped perovskite ferrate as an efficient anode of a solid oxide fuel cell with in situ metal exsolution," *Journal of Materials Chemistry A,* vol. 7, no. 47, pp. 26944-26953, 2019.

[7] Z. Wei *et al.*, "3D network-structured CoSb/P-CNFs@ rGO as a highly conductive self-supporting anode material for lithium-ion batteries," *Journal of Alloys and Compounds,* vol. 960, p. 170763, 2023.

[8] B. Mazhar, A. Ali, F. Anwer, M. Majeed, and R. Raza, "Catalytic effect of aluminum on the structural, optical, and electrical properties of LaSrCrO3-δ anode," *Ceramics International,* vol. 50, no. 13, pp. 23088-23096, 2024.

[9] S.-x. Yan *et al.*, "Rational design of flower-like FeCo2S4/reduced graphene oxide films: Novel binder-free electrodes with ultra-high conductivity flexible substrate for high-performance all-solid-state pseudocapacitor," *Chemical engineering journal,* vol. 381, p. 122695, 2020.

[10] X. Zhang *et al.*, "Porous and graphitic structure optimization of biomass-based carbon materials from 0D to 3D for supercapacitors: A review," *Chemical Engineering Journal,* vol. 460, p. 141607, 2023.

[11] M. Z. Iqbal and U. Aziz, "Supercapattery: Merging of battery-supercapacitor electrodes for hybrid energy storage devices," *Journal of Energy Storage,* vol. 46, p. 103823, 2022.

[12] M. A. Kamran, K. Rasheed, S. Ullah, W. Ali, S. M. Ali, and M. H. Aziz, "Tailoring electrochemical and dielectric properties of SrO nanostructures through Cr-doping for energy storage applications," *Materials Today Communications,* vol. 38, p. 107925, 2024.

[13] N. Duraisamy *et al.*, "Development of asymmetric device using Co3 (PO4) 2 as a positive electrode for energy storage application," *Journal of Materials Science: Materials in Electronics,* vol. 30, no. 8, pp. 7435-7446, 2019.

[14] A. Khorate and A. V. Kadam, "An overview of patents and recent development in flexible supercapacitors," *Journal of Energy Storage,* vol. 52, p. 104887, 2022.

[15] M. A. Kamran *et al.*, "Boosting electrochemical and photocatalytic performance of Cadmium Sulfide/Zinc Telluride nanocomposites via Nickel doping," *Materials Science and Engineering: B,* vol. 299, p. 116932, 2024.

[16] S. Yasami, S. Mazinani, and M. Abdouss, "Developed composites materials for flexible supercapacitors electrode:"Recent progress & future aspects"," *Journal of Energy Storage,* vol. 72, p. 108807, 2023.

[17] A. E. Elkholy, F. E.-T. Heakal, and N. K. Allam, "A facile electrosynthesis approach of amorphous Mn-Co-Fe ternary hydroxides as binder-free active electrode materials for high-performance supercapacitors," *Electrochimica Acta,* vol. 296, pp. 59-68, 2019.

[18] N. Ahmed, B. A. Ali, M. Ramadan, and N. K. Allam, "Three-dimensional interconnected binder-free Mn–Ni–S nanosheets for high performance asymmetric supercapacitor devices with exceptional cyclic stability," *ACS Applied Energy Materials,* vol. 2, no. 5, pp. 3717-3725, 2019.

[19] M. M. Mubasher, A. Bashir, M. Rashid, T. Umar, Z. Sarfraz, and H. Zia, "Barium doping effects on frequency-dependent dielectric properties of cobalt ferrite nanoparticles," *Materials Innovations,* vol. 2, no. 3, pp. 1-10, 2022.

[20] M. Z. Iqbal *et al.*, "Capacitive and diffusion-controlled mechanism of strontium oxide based symmetric and asymmetric devices," *Journal of Energy Storage,* vol. 27, p. 101056, 2020.

[21] M. Z. Iqbal *et al.*, "Binary composites of strontium oxide/polyaniline for high performance supercapattery devices," *Solid State Ionics,* vol. 347, p. 115276, 2020.

[22] M. Z. Iqbal *et al.*, "Strontium phosphide-polyaniline composites for high performance supercapattery devices," *Ceramics International,* vol. 46, no. 8, pp. 10203-10214, 2020.

[23] M. A. Kamran *et al.*, "Bifunctional strontium-doped barium oxide nanorods as promising photocatalysts and electrodes for energy storage applications," *Journal of Energy Storage,* vol. 67, p. 107598, 2023.

[24] V. Molahalli, K. Chaithrashree, M. K. Singh, M. Agrawal, S. G. Krishnan, and G. Hegde, "Past decade of supercapacitor research–lessons learned for future innovations," *Journal of Energy Storage,* vol. 70, p. 108062, 2023.

[25] R. Xie, H. Huang, X. Qi, and G. Wei, "Significant enhancement of the electrochemical performance of hierarchical Co3O4 electrodes for supercapacitors via architecture design and training activation," *Journal of Energy Storage,* vol. 35, p. 102258, 2021.

[26] R. D. Kumar *et al.*, "High-performance chrysanthemum flower-like structure of Ni doped ZnO nanoflowers for pseudo-supercapacitors," *Journal of Energy Storage,* vol. 72, p. 108441, 2023.

[27] T. Liu *et al.*, "Metal-organic framework derived porous ternary ZnCo2O4 nanoplate arrays grown on carbon cloth as binder-free electrodes for lithium-ion batteries," *Chemical Engineering Journal,* vol. 354, pp. 454-462, 2018.

[28] S. Peng, L. Li, H. B. Wu, S. Madhavi, and X. W. Lou, "Controlled growth of NiMoO4 nanosheet and nanorod arrays on various conductive substrates as advanced electrodes for asymmetric supercapacitors," *Advanced Energy Materials,* vol. 5, no. 2, p. 1401172, 2015.

[29] D. Guo *et al.*, "Facile synthesis and excellent electrochemical properties of CoMoO4 nanoplate arrays as supercapacitors," *Journal of Materials Chemistry A,* vol. 1, no. 24, pp. 7247-7254, 2013.

[30] H. Liu, D. Zhao, Y. Liu, P. Hu, X. Wu, and H. Xia, "Boosting energy storage and electrocatalytic performances by synergizing CoMoO4@ MoZn22 core-shell structures," *Chemical Engineering Journal,* vol. 373, pp. 485-492, 2019.

[31] S. Baskar, D. Meyrick, K. S. Ramakrishnan, and M. Minakshi, "Facile and large scale combustion synthesis of α-CoMoO4: Mimics the redox behavior of a battery in aqueous hybrid device," *Chemical Engineering Journal,* vol. 253, pp. 502-507, 2014.
[32] I. Shaheen, K. S. Ahmad, C. Zequine, R. K. Gupta, A. Thomas, and M. A. Malik, "Organic template-assisted green synthesis of CoMoO4 nanomaterials for the investigation of energy storage properties," *RSC advances,* vol. 10, no. 14, pp. 8115-8129, 2020.
[33] X. Xia, W. Lei, Q. Hao, W. Wang, and X. Wang, "One-step synthesis of CoMoO4/graphene composites with enhanced electrochemical properties for supercapacitors," *Electrochimica Acta,* vol. 99, pp. 253-261, 2013.
[34] F. Nti, D. A. Anang, and J. I. Han, "Facilely synthesized NiMoO4/CoMoO4 nanorods as electrode material for high performance supercapacitor," *Journal of Alloys and Compounds,* vol. 742, pp. 342-350, 2018.
[35] J. Wang *et al.*, "3D self-supported nanopine forest-like Co3O4@ CoMoO4 core–shell architectures for high-energy solid state supercapacitors," *Nano Energy,* vol. 19, pp. 222-233, 2016.
[36] M. A. Kamran, W. Ali, S. Ullah, T. Alharbi, and Q. Gul, "Facile preparation of Ga-doped ZnO nanostructures by composite-hydroxide-mediated synthesis route for high-performance pseudocapacitors," *Journal of Energy Storage,* vol. 62, p. 106871, 2023.
[37] K. A. Ben Brahim *et al.*, "Electrochemical detection of sulfadiazine by sensors based on chemically modified carbon electrodes: A review," *Current Topics in Medicinal Chemistry,* vol. 23, no. 15, pp. 1464-1476, 2023.
[38] L. Li *et al.*, "Coral-like CoMoO4 hierarchical structure uniformly encapsulated by graphene-like N-doped carbon network as an anode for high-performance lithium-ion batteries," *Journal of colloid and interface science,* vol. 586, pp. 11-19, 2021.
[39] T. Ma, Y. Wu, N. Liu, X. Tao, and Y. Wu, "Iron-doped g-C3N4 modified CoMoO4 as an efficient heterogeneous catalyst to activate peroxymonosulfate for degradation of organic dye," *Journal of Dispersion Science and Technology,* vol. 43, no. 1, pp. 80-93, 2021.
[40] S. Feng and R. Xu, "New materials in hydrothermal synthesis," *Accounts of chemical research,* vol. 34, no. 3, pp. 239-247, 2001.
[41] T. Yang, H. Zhang, L. Mei, D. Guo, Q. Li, and T. Wang, "Enhanced electrochemical performance of CoMoO4 nanorods/reduced graphene oxide as anode material for lithium-ion batteries," *Electrochimica Acta,* vol. 158, pp. 327-332, 2015.
[42] X. Yan, L. Tian, S. Atkins, Y. Liu, J. Murowchick, and X. Chen, "Converting CoMoO4 into CoO/MoO x for overall water splitting by hydrogenation," *ACS Sustainable Chemistry & Engineering,* vol. 4, no. 7, pp. 3743-3749, 2016.
[43] C. V. M. Gopi, S. Sambasivam, K. V. G. Raghavendra, R. Vinodh, I. M. Obaidat, and H.-J. Kim, "Facile synthesis of hierarchical flower-like NiMoO4-CoMoO4 nanosheet arrays on nickel foam as an efficient electrode for high rate hybrid supercapacitors," *Journal of Energy Storage,* vol. 30, p. 101550, 2020.
[44] X. Ma *et al.*, "Self-supported phosphorus-doped CoMoO4 rod bundles for efficient hydrogen evolution," *Journal of Materials Science,* vol. 55, no. 15, pp. 6502-6512, 2020.
[45] U. Holzwarth and N. Gibson, "The Scherrer equation versus the'Debye-Scherrer equation'," *Nature nanotechnology,* vol. 6, no. 9, pp. 534-534, 2011.
[46] K. Hedayati, A. Zendehnam, and F. Hassanpour, "Fabrication and characterization of zinc sulfide nanoparticles and nanocomposites prepared via a simple chemical precipitation method," *Journal of Nanostructures,* vol. 6, no. 3, pp. 207-212, 2016.
[47] J. Zhu, S. Liu, O. Palchik, Y. Koltypin, and A. Gedanken, "A novel sonochemical method for the preparation of nanophasic sulfides: synthesis of HgS and PbS nanoparticles," *Journal of Solid State Chemistry,* vol. 153, no. 2, pp. 342-348, 2000.
[48] L. Fang *et al.*, "Hierarchical CoMoO4 nanoneedle electrodes for advanced supercapacitors and electrocatalytic oxygen evolution," *Electrochimica Acta,* vol. 259, pp. 552-558, 2018.
[49] Y. Zhang *et al.*, "Structural evolution of CoMoO4 to CoOOH by ion electrochemical etching for boosting oxygen evolution reaction," *Journal of Power Sources,* vol. 442, p. 227252, 2019.
[50] J. Xu, S. Gu, L. Fan, P. Xu, and B. Lu, "Electrospun lotus root-like CoMoO4@ graphene nanofibers as high-performance anode for lithium ion batteries," *Electrochimica Acta,* vol. 196, pp. 125-130, 2016.
[51] B. Liu and H. C. Zeng, "Hydrothermal synthesis of ZnO nanorods in the diameter regime of 50 nm," *Journal of the American Chemical Society,* vol. 125, no. 15, pp. 4430-4431, 2003.
[52] R. K. Selvan, I. Perelshtein, N. Perkas, and A. Gedanken, "Synthesis of hexagonal-shaped SnO2 nanocrystals and SnO2@ C nanocomposites for electrochemical redox supercapacitors," *The Journal of Physical Chemistry C,* vol. 112, no. 6, pp. 1825-1830, 2008.
[53] R. López and R. Gómez, "Band-gap energy estimation from diffuse reflectance measurements on sol–gel and commercial TiO2: a comparative study," *Journal of sol-gel science and technology,* vol. 61, no. 1, pp. 1-7, 2012.
[54] W. Li *et al.*, "Hydrothermal synthesized of CoMoO4 microspheres as excellent electrode material for supercapacitor," *Nanoscale Research Letters,* vol. 13, no. 1, p. 120, 2018.
[55] Q. Meng, K. Cai, Y. Chen, and L. Chen, "Research progress on conducting polymer based supercapacitor electrode materials," *Nano Energy,* vol. 36, pp. 268-285, 2017.
[56] Y. Zhang *et al.*, "NiMoO4 nanorods supported on nickel foam for high-performance supercapacitor electrode materials," *Journal of Renewable and Sustainable Energy,* vol. 10, no. 5, 2018.
[57] S. Rajkumar, M. Karthikeyan, A. Manohar, S. Dhineshkumar, and J. P. Merlin, "One-step synthesis and fabrication of ZrMo2O8 nanostructures as advanced electrode material for energy storage applications," *Journal of Industrial and Engineering Chemistry,* vol. 137, pp. 162-173, 2024.
[58] L. Wang *et al.*, "Electrochemical impedance spectroscopy (EIS) study of LiNi1/3Co1/3Mn1/3O2 for Li-ion batteries," *International Journal of Electrochemical Science,* vol. 7, no. 1, pp. 345-353, 2012.